Aeroacoustics Conferences
June 14-17, 2022, Southampton, UK
28th AIAA/CEAS Aeroacoustics 2022 Conference

10.2514/6.2022-2838



# Investigation of small-scale rotor aeroacoustic in DLR's acoustic Wind Tunnel Braunschweig

Karl-Stéphane Rossignol*, Jianping Yin† and Lukas Rottmann‡
*German Aerospace Center, Braunschweig, 38108, Germany*

**This paper presents a multi-rotor test rig designed for the investigation of the aerodynamics and acoustics of small-scale propellers, relevant for urban air mobility vehicles applications. The test rig allows testing of isolated rotors, rotors in coaxial configurations and rotors in tandem configurations in various parametric combinations. Selected results are presented to emphasize the impact of aerodynamic and acoustic interaction effects on the characteristics of the acoustic emissions from multi-rotor configurations. The results indicate that amplification of harmonics and sub-harmonics noise components in the mid- to high-frequency range as well an increased broadband noise component are to be expected for such configurations. The work presented herein constitutes a first effort to experimentally investigate small-scale rotors to provide a database for the validation of numerical simulation schemes.**



## I. Nomenclature

| | | |
|---|---|---|
| $D$ | = | Rotor diameter, [m] |
| $U_\infty$ | = | Free-stream velocity, [m/s] |
| $\theta$ | = | Observer elevation angle, [°] |
| $\alpha$ | = | Shaft angle, [°] |
| $\alpha_b$ | = | Effective blade angle of attack, [°] |
| $R$ | = | Observer distance, [m] |
| $F$, $F_x$, $F_y$, $F_z$ | = | Force, [N] |
| $M$, $M_x$, $M_y$, $M_z$ | = | Moment, [N] |
| $Ma_t$ | = | Blade tip Mach number, [-] |
| $A_R$ | = | Rotor area, [m$^2$] |
| $R_R$ | = | Rotor radius, [m] |
| $\Omega$ | = | Rotor rotation frequency, [rad/s] |
| $C_T = \frac{F}{\rho A_R (\Omega R_R)^2}$ | = | thrust coefficient, [-] |
| $C_Q = \frac{M}{\rho A_R (\Omega R_R)^2 R_R}$ | = | torque coefficient, [-] |
| $FM = \frac{C_T^{\frac{3}{2}}}{\sqrt{2} C_Q}$ | = | Figure of Merit, [-] |
| $x$, $y$, $z$ | = | Body-fixed coordinates [m] |
| $x'$, $y'$, $z'$ | = | Wind tunnel coordinates [m] |

## II. Introduction

In the context of a growing interest in the development of urban air mobility (UAM) solutions to city transport congestion problems, comes the necessity to provide answers to fundamental questions regarding the aerodynamic and acoustic characteristics of these new vehicles [1, 2].

Urban Air Vehicles (UAVs) or Urban Air Mobility Vehicles (UAMVs) usually refers to small aircraft capable of transporting one to five passengers for intercity transportation. They feature vertical take-off and landing (VTOL) capability through a distributed, ducted or open, multi-rotor propulsion systems. Usually open rotors are selected which

*Research Scientist, Institute of Aerodynamics and Flow Technology, karl-stephane.rossignol@dlr.de, AIAA Senior Member
†Research Scientist, Institute of Aerodynamics and Flow Technology
‡Research Scientist, Institute of Aerodynamics and Flow Technology

are significant sources of tonal and broadband noise. Due to their smaller scales, compared to helicopter rotors and aircraft propellers, broadband noise components will have a greater importance in the overall sound emission as blade tip Mach numbers on the order of 0.2 to 0.5 can be reached. Thus tonal source components are expected to be important only for the first few harmonics. Currently, many different vehicle designs have been proposed (such as the city Airbus, Volocopter and EHang), and a general prediction of the acoustic emission characteristics of a specific design remain a difficult task. The use of distributed propulsion systems as well tilt-rotor configurations poses issues related to acoustic installation effects, which may lead to unwanted secondary sources. As a consequence of source-source interaction and/or source-airframe interactions.

Insights into aspects of aerodynamics and acoustics of these vehicles can be gathered through dedicated fly-over measurements and wind tunnel experiments [3, 4]. Ultimately the collected data will provide the foundation necessary for the elaboration of semi-empirical acoustic prediction schemes. It will also serve to validate and improve current numerical simulation methodologies, both with respect to aerodynamics and aeroacoustics.

The aim of the present contribution is to provide details of the experimental methodology followed at DLR for the investigation of the acoustic and aerodynamic characteristics of rotors relevant to small-scale UAVs and by extension to UAM applications. The rig design is presented along with information on the electronic components selected to drive the rotors and the available instrumentation. Selected results are presented to emphasize the operating range of the test rig.



## III. Experimental Setup

The investigations were conducted in the Acoustic Wind Tunnel Braunschweig (AWB) [5], e.g. Fig. 1. It is DLR's small size high-quality anechoic testing facility. It is an open-jet Göttingen-type wind tunnel capable of running at speeds of up to 65 m/s and optimized for noise measurements at frequencies above 250 Hz. The nozzle is 1.2 m high by 0.8 m in width. The AWB has been in service since the 1970s and is used to conduct research on a wide range of topics, from classical airframe noise problems to propeller/rotor noise, as well as jet installation noise and noise shielding problems. The AWB is equipped with most standard means for the realization of acoustic measurements, as well as basic aerodynamic measurements. A special support was designed to extend the capabilities of the facility to meet the requirements of simultaneous measurements of multiple rotors under static and flight conditions, e.g. Fig. 2 and Fig. 3.

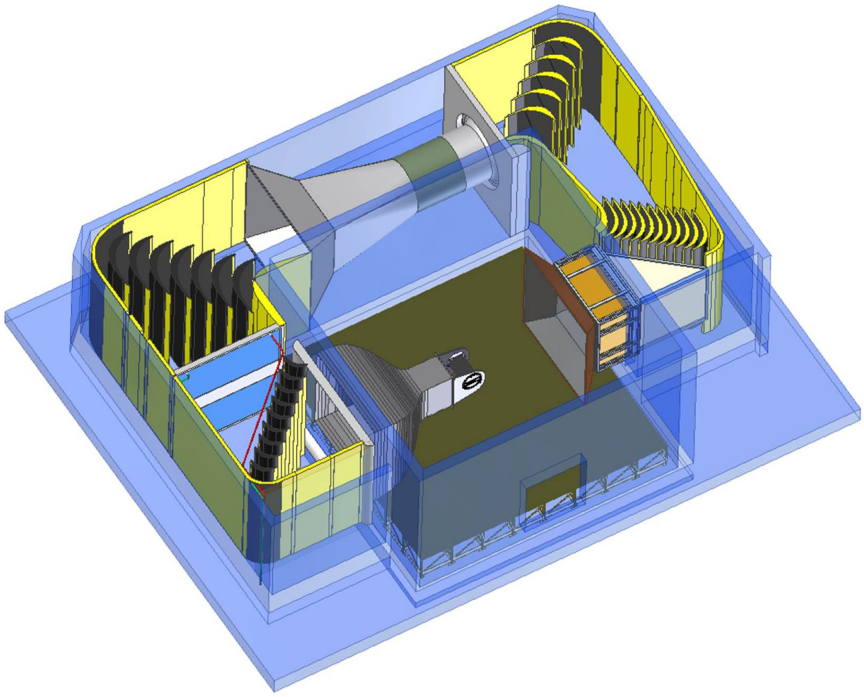

**Fig. 1 Acoustic Wind Tunnel Braunschweig (AWB)**

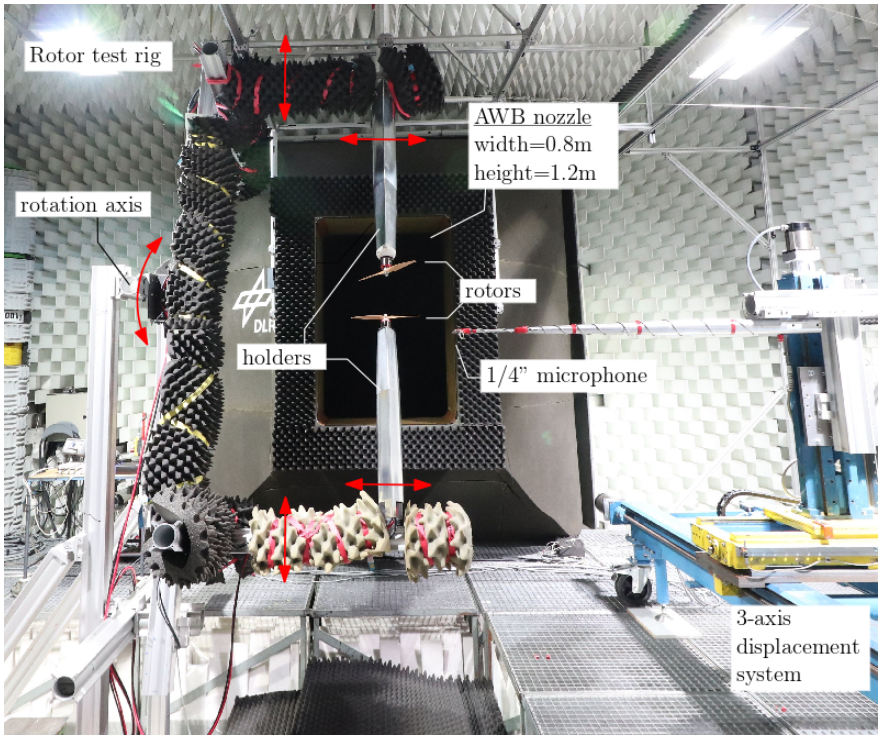


**Fig. 2 Rotor test setup in AWB. Red arrows indicates movable parts of the rig.**

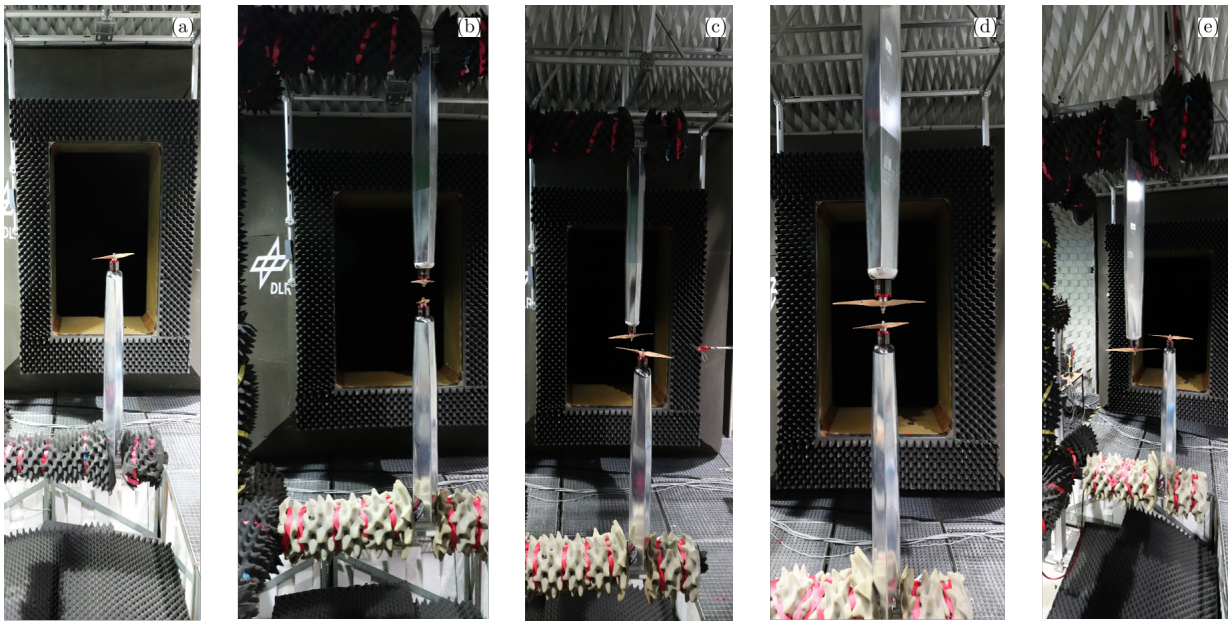


**Fig. 3 Rotor configurations. (a) Isolated, (b) Coaxial, (c) Tandem, (d) Tandem (vertical offset), (e) Tandem (lateral offset)**

### A. Electronics

Using this setup, several propeller configurations can be investigated; isolated, coaxial, tandem with vertical and lateral offset as shown in Fig. 3. Rotors with a diameter of up to 0.4 m can be tested. The rotors are propelled by 14-poles Leopard LC5065 brushless motors with 0.2 mm stator plates and 520 U/min/V. The motor was controlled with

YGE 205HVT speed controllers, capable of a theoretical maximal RPM of 34283 min$^{-}$1, and SM300-Series 3300 W DC power supplies. The motors can deliver a maximum power of 2.1 kW. The power supplies allow a maximum tension of 30 V and correspondingly, a maximum current of 70 A. This combination allows RPM up to 13000 to be reached with an installed propelled. Without mounted propeller, a maximum RPM of 15600 would be theoretically achievable.

Each propeller holder is equipped a speed controller, a six-components load cell, a Hall-effect RPM sensor and a motor. An aluminum block spacer provides enough space between the motor and the load cell to insure low thermal and electromagnetic perturbations on the load cell's output, e.g. Fig. 8. The RPM sensor is mounted on the motor axle to provide independent direct measurements of each motor's RPM. Both the RPM signal and the acoustic signals are acquired in a synchronously. The propellers are mounted to the motors through a screw adapter.

### B. Coordinate Systems

Two coordinate systems are defined in Fig. 4, for the single rotor configuration, and in Fig. 5 for the coaxial and tandem configurations. The ($x'$, $y'$, $z'$) axes correspond to the wind tunnel fixed coordinates while the ($x$, $y$, $z$) axes are body-fixed coordinates. The shaft angle ($\alpha$) of the propeller defines the rotation between both coordinate systems. Depending on the configuration considered, a different origin for the coordinates systems is defined. For the single propeller configuration, the origin is set on the rotor axle at the blade tip level in $z$. For the coaxial configuration (e.g. Fig. 5 left), the origin lies at middle point between each rotor in $z$, centered on both axles in the $x - y$ plane. For the tandem configuration (e.g. Fig. 5 right), the origin lies at the mid-point between both rotor axle in $x$ and $y = 0$ m with $z = 0$ m leveled with the front rotor blade's tip height.

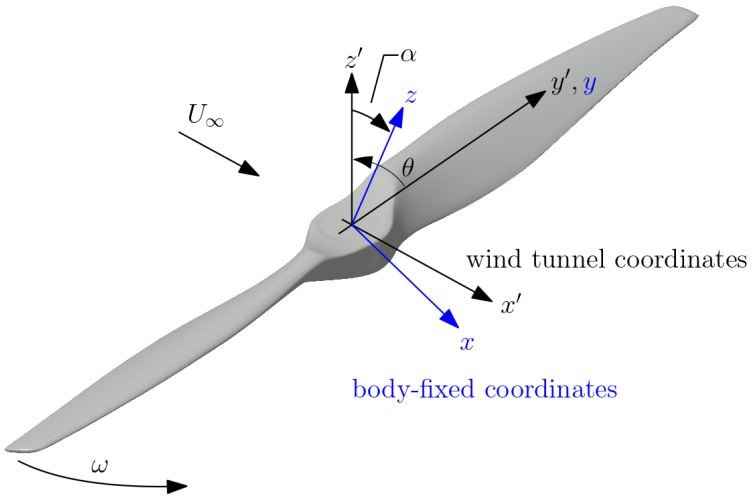


**Fig. 4 Coordinate system definition for the isolated rotor configuration**

### C. Force, Moment and RPM Measurement Aparatus

For each rotor, performance data, in terms of thrust and torque, is acquired through miniature six-components load cells, Model K6D40 from ME-Meßsysteme GmbH Germany, mounted beneath the motors. The load cells are separated from the motors by an aluminum block spacer to reduce as much as possible the influence of temperature variations and that of the motor's electromagnetic field on the measurements. The load cells are strain-gauge-based instruments which measure three orthogonal forces ($F_x$, $F_y$, $F_z$) and three orthogonal moments ($M_x$, $M_y$, $M_z$). The load cells were factory calibrated by the manufacturer to a full-scale thrust $F_z = 200$ N ($F_x = F_y = 50$ N) and a full-scale torque $M_z$ of 5 Nm. The load cell signals are sampled at a rate 5 Hz by the manufacturer-provided pre-conditioning amplifier box. The manufacturer's data sheet rates the load cell with a precision of 0.2% full-scale, corresponding to 0.4 N. Preliminary investigations have shown that this value is strongly dependent on temperature variations and is also RPM dependent, i.e. load dependent. A conservative estimate of the bias error on the load measurement is 0.5% full-scale, though in the experiment this error was minimized through frequent zeroing of the load cells and short measurement time. The precision of the load cells is within the range given by the manufacturer (i.e. 0.2% full-scale).

Each rotor RPM is acquired through a 1/rev signal generated by a Hall-effect sensor mounted to the rotor's shaft.

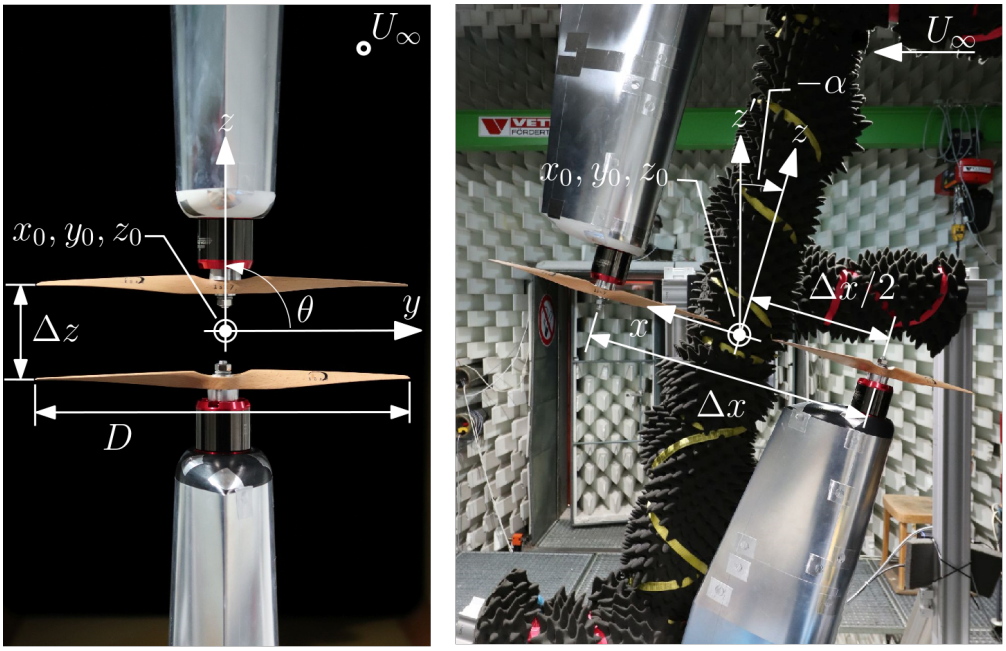


**Fig. 5 Coordinate system definition for the coaxial (left) and tandem (right) rotor configurations (body-fixed coordinates).**

This signal also serves as a trigger signal to phase lock the acoustic data later in post-processing. The acquisition of the load signals is done synchronously with the acquisition of the microphone and Hall-effect sensor (RPM) signals at a sampling rate of 100 kHz.

The good steadiness of the RPM and load measurements over the course of a measurement is displayed in figure 6 for a single rotor in hover and RPM=12000, for a blade passing frequency of 391.4 Hz. The results of Fig. 6 are presented in terms of narrow band sound pressure level, i.e. SPL vs. Frequency and as a spectrogram, i.e. SPL vs. time for a microphone located below the rotor plane at $\theta = -30°$. For this particular position harmonic sound components are found to dominate at low frequency while broadband noise become more important for frequencies greater than 5 kHz. These results suggest that there are no prevalent issues related unsteady flow recirculation inside the test section. The stability of the results over time is also a confirmation that the selected electronics are appropriate to run tests at high RPMs over a sufficient period of time to ensure the acquisition of high number of data blocks for statistical analysis.

### D. Acoustic Measurement Aparatus

The rotor's acoustic emission was acquired through a single 1/4" GRAS 40 DP pressure field microphone mounted to a 3-axis linear displacement system (e.g. Fig. 2). The microphone was placed in the flow field with its membrane protected by a Brüel und Kjær nose cap. The microphone was aligned parallel to the flow field with its sensing surface pointing upstream. Although numerous microphone positions were utilized in the experiment, for the purpose of the present paper we will focus on a single measurement position, in the $y - z$ plane and at an observer elevation angle of $\theta = -30°$ (e.g. Fig. 4).

The acoustic signal, along with the 1/rev signal, is sampled at a 100 kHz rate on a GMB Viper GmbH 48 channel data acquisition unit. A high-pass digital filter is used to remove low frequency noise contamination due to the wind tunnel flow. The filter characteristic is removed in the data processing steps. The processing takes advantage of the 1/rev signal to phase-lock the data on a revolution per revolution basis prior to spectral and time domain analysis. Each data block is normalize to a unit revolution time to account for fluctuations in total revolution sample count. The typical standard deviation of the sample count per revolution is on the order of 1 to 2 samples, i.e. 10 $\mu$s - 20 $\mu$s, depending on the configuration and RPM, with lower RPM showing smaller variations. At a RPM of 8000, one revolution counts on average 748 samples, while at a RPM of 12000 this count reduced to 500 samples. Prior to Fourier analysis, the 32 individual blocks, i.e. revolutions, are stacked together to form a sufficiently long time sequence to achieve a high frequency resolution. Each time series is then Fourier transformed using a Hanning window to minimize spectral

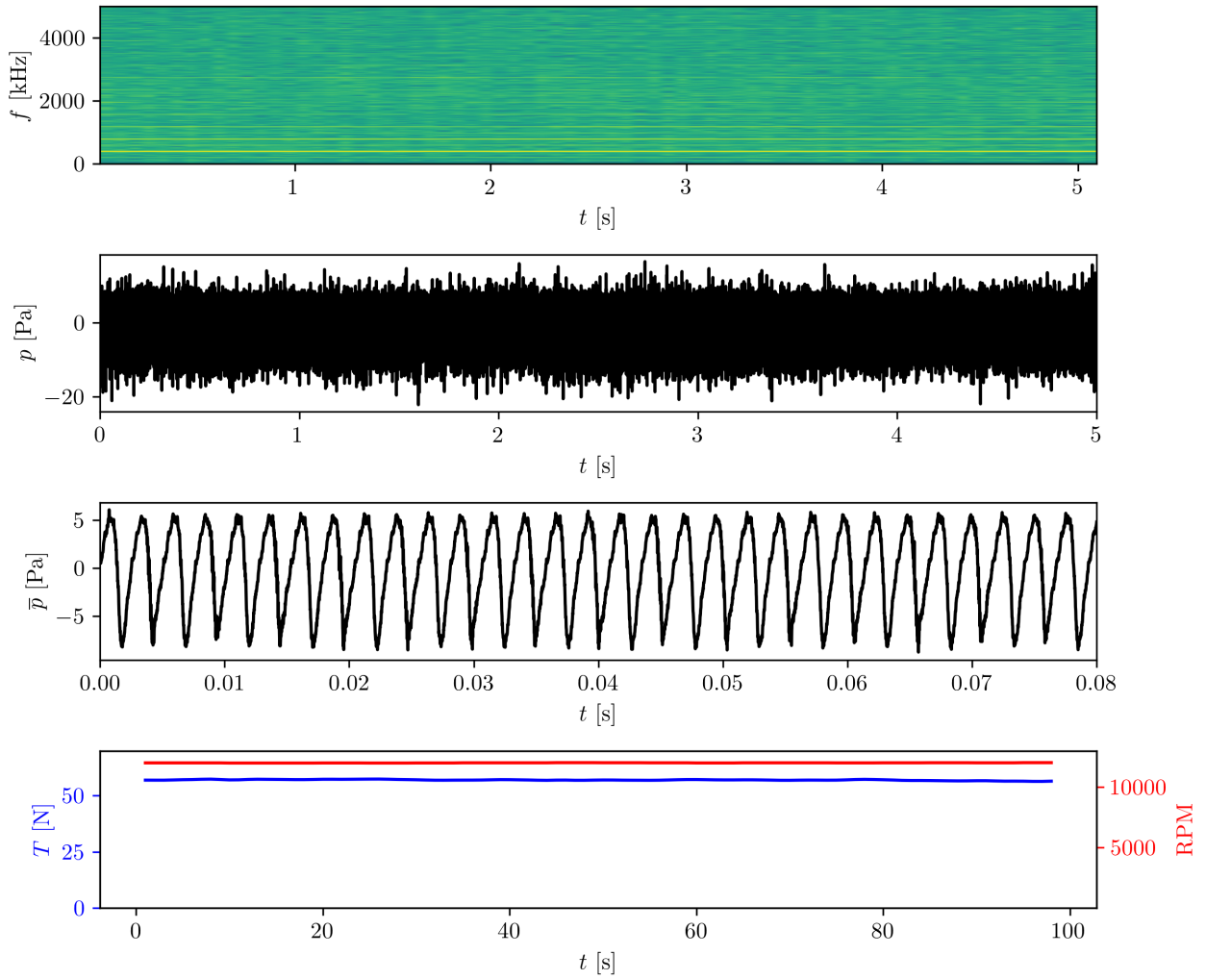


**Fig. 6 Spectrogram and time histories of the acoustic pressure, thrust and RPM. Single rotor, RPM=12000, $U_\infty = 0$ m/s, $\alpha = 0°$ and $\theta = -30°$. From the top, 1) spectrogram, 2) instantaneous acoustic pressure, 3) averaged acoustic pressure and 4) Thrust and RPM.**

leakage issues. Averaged spectra are obtained through ensemble averaging of individual spectra and through time domain ensemble averaging prior to the Fourier analysis step. Spectral averaging preserves the broadband content of the signals, whereas time domain averaging tends to reduce it due to its incoherent nature and thus emphasize the harmonic components.

In figure 7, the signal-to-noise ratio (SNR) is analysed for representative configurations and operating conditions. Rotor harmonic and broadband noise is found to be dominant over most of the frequency range of interest. The unloaded motor noise, i.e. with the blade removed, is shown in green in all plots. In this configuration, motor noise overwhelms the rotor contributions only at specific harmonics. When the rotor is mounted, its contribution is expected to manifest itself in the sub-harmonics. A further contribution to the sub-harmonics originates from the geometric asymmetry of the blade used in the experiment. At RPM=8000, the SNR drops significantly and the contamination of the signal through motor noise is expected to be important. Background flow noise is due to the wind tunnel jet but also due to flow interaction with the in-flow microphone. For the single rotor case, flow noise is found to be gain in level below 500 Hz while remaining well below the rotor contribution. For the coaxial and tandem configurations, flow noise does, however, greatly increases leading to worsening of the SNR especially 1.5 kHz and more so for the lower RPM cases (e.g. Fig. 7d).

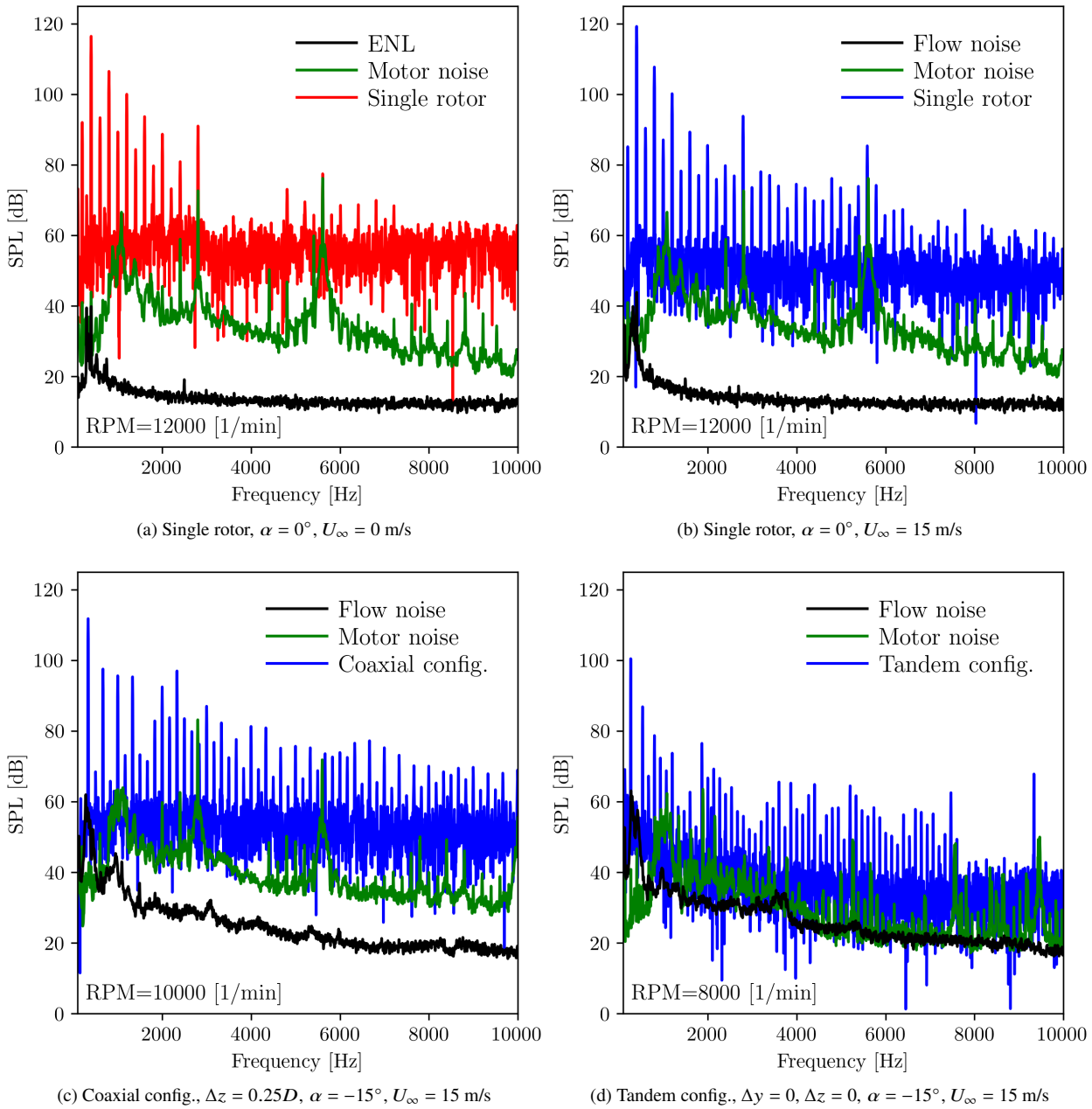


(a) Single rotor, $\alpha = 0°$, $U_\infty = 0$ m/s

(b) Single rotor, $\alpha = 0°$, $U_\infty = 15$ m/s

(c) Coaxial config., $\Delta z = 0.25D$, $\alpha = -15°$, $U_\infty = 15$ m/s

(d) Tandem config., $\Delta y = 0$, $\Delta z = 0$, $\alpha = -15°$, $U_\infty = 15$ m/s

**Fig. 7 Signal to noise ratio vs rotor configuration and operating conditions.**

## IV. Aerodynamic Results of the Preliminary Investigations

The electronic equipment was first tested in a preliminary test. Figure 8 shows the setup of the preliminary test. Only the test section of the AWB was used, the wind tunnel was not in action. In the preliminary tests, a number of propellers were examined in hover flight in order to make a selection of propellers for the main test. Commercial model propellers from the manufacturer Xoar were used. The propellers are made of wood and have a diameter of 13 inches or 0.33 m due to the limited size of the wind tunnel nozzle. The propellers used differ only in their pitch and direction of rotation. Four different pitch angles were used: 7, 6.5, 5, 4 inches. The pitch of the propeller is defined as the distance the propeller would travel during a full rotation of 360°. This means that the greater the pitch, the steeper the blades of the propeller are pitched. Right and left turning propellers of each propeller of a specific pitch have been investigated. The right and left rotating propellers are mirrored along the span and thus generate an equal thrust vector for their

direction of rotation.

Figure 9 left shows the dimensionless thrust coefficient versus blade tip mach number for the right spinning propellers. The results for the left spinning propellers are similar. Comparing the CT values at different tip mach numbers for the propellers with a pitch of 4.5 to 6.5 inch shows that the higher the pitch, the higher the thrust. The propeller with pitch 7 inch shows an increase in thrust only for small tip Mach numbers and for a range at large tip Mach numbers compared to pitch 6.5 inch. This suggests that the maximum pitch for this flight condition has been reached or even exceeded, e.g. flow separation may occur for the higher pitch (7 inches) blades corresponding with the high torque coefficients identified in Fig. 9. Furthermore, it can be seen that the propellers are not independent of the tip Mach number, rather the thrust coefficient varies across the tip Mach number due to aerodynamic effects, for example the Reynolds number. Figure 9 right visualizes the dimensionless torque coefficient. Here it can also be seen that the drag of the propeller and thus the torque increases with increasing pitch. Compared to the thrust coefficient, the torque coefficient is less dependent on the blade tip Mach number. Figure 10 shows the Figure of Merit (FM). FM represents the ratio of the ideal propeller to the measured propeller and can be understood as a performance quality number. The propellers achieve a maximum efficiency of 35%. Whereas low pitch propellers have their FM maximum at high tip Mach numbers, high pitch propellers have their maximum at medium tip Mach numbers. This can be explained by the fact that the thrust coefficient decreases with increasing tip Mach number for propeller pitch greater than 5 inches and the moment coefficient increases at the same time.

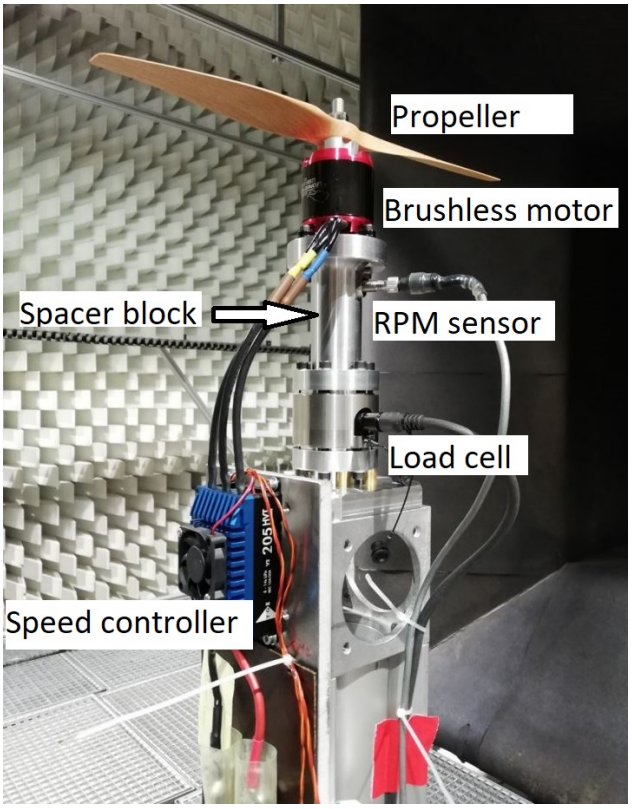


**Fig. 8 Details of the setup's electronics in preliminary test**

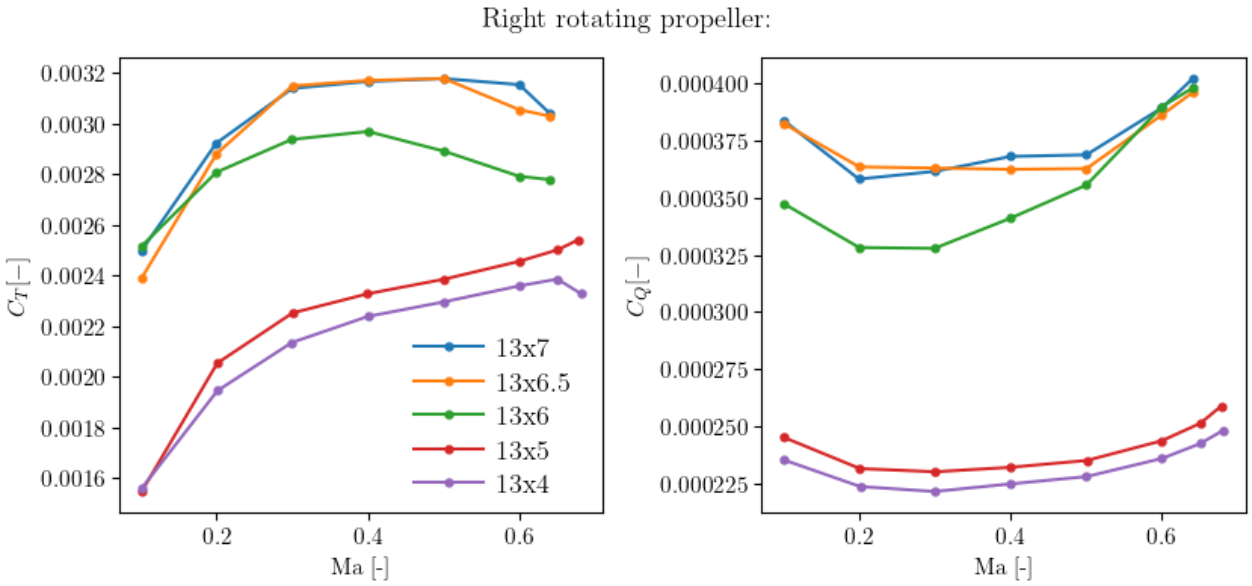


**Fig. 9 Left: Thrust coefficient over Tip mach number. Right: Torque coefficient over Tip mach number**

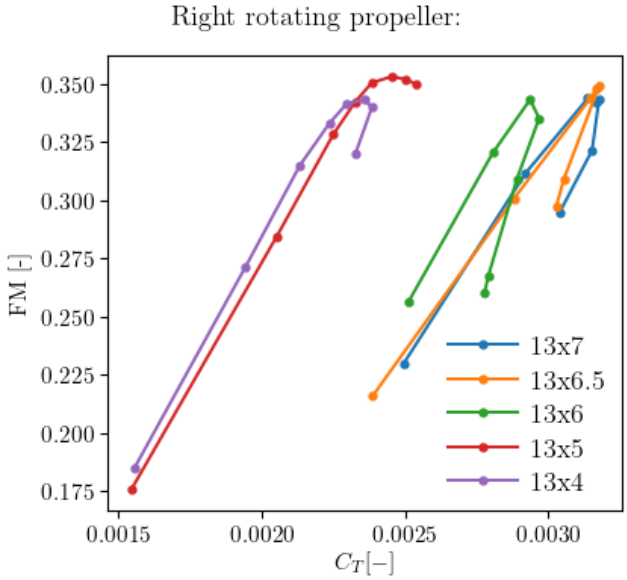


**Fig. 10 figure of merit over thrust coefficient**

## V. Acoustic Results

In this section, selected acoustic results are presented. The presentation will focus on results obtained at microphone location $\theta = -30°$ in the $y - z$ plane, e.g. Fig. 4. From the discussion of the previous section, the 13x7 right-handed rotor blade was selected as it provides the largest thrust over a wide RPM range, and thus a better acoustic SNR compared to the other blades. The discussion will, for the most part, deal with spectral-averaged data to better emphasize the relative importance of both the broadband and tonal components of the source. Plots of the time-averaged data are also provide in the appendix for reference, and will be referred to as needed.

### A. Isolated Rotor

The isolated rotor case provides the baseline configuration to which the double rotor configurations will later be compared to. The aim is not at a case-to-case quantitative comparison but rather at a qualitative evaluation of the relative weighting of the tonal and broadband components for each configuration.

Spectra for the forward climb flight and forward decent cases for RPM=12000 are presented in figure 11 for two free-stream velocities. Most of the tonal components energy is concentrated in the first few harmonics. For this specific RPM, motor noise clearly stands out in the 2.8 kHz band. For the forward flight case, a reduction in harmonics levels above 3 kHz can be observed which relates to the reduction of the effective blade angle of attack ($\alpha_b$) at this shaft angle, e.g. Section IV. In the decent mode, the rotor torque increase due to the incoming flow direction change increasing $\alpha_b$ and more thrust is produced. This, in turns, leads to an increased acoustic emissions above 1 kHz for both the tonal and broadband components, broadband noise being more strongly affected.

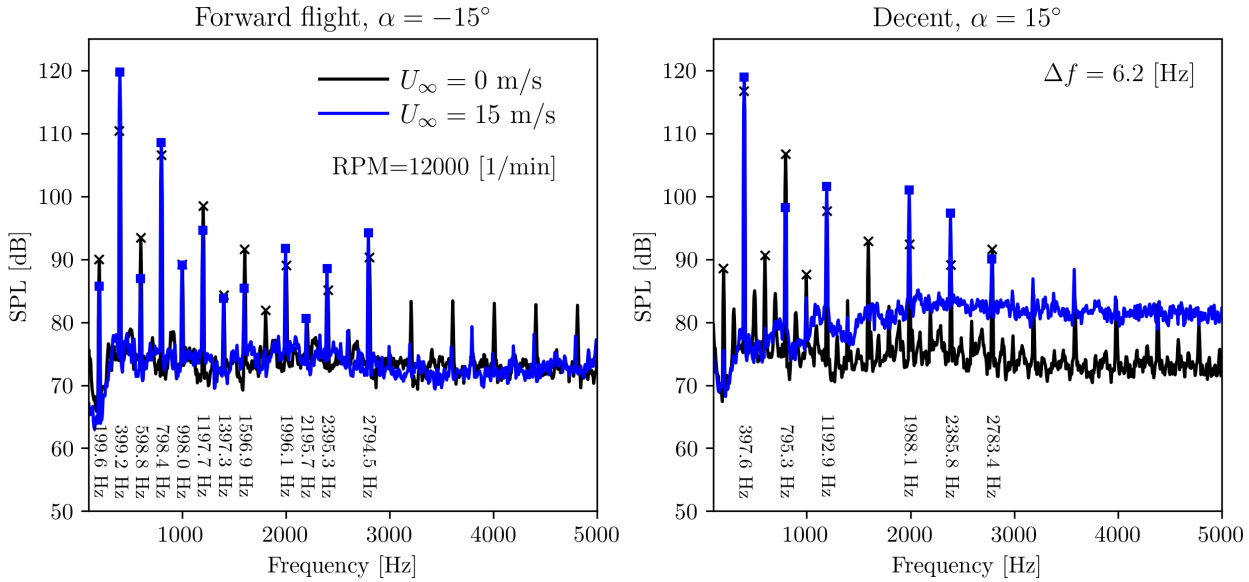


**Fig. 11 Single rotor configuration. Effect of shaft angle and free-stream velocity on the acoustic radiation. Spectral averaging to emphasize the broadband noise component. RPM=12000 1/min, $\theta = -30°$, $R = 0.3$ m.**

### B. Coaxial Configuration

Spectral-averaged spectra for two coaxial configurations are presented in Fig. 12 ($\Delta z = 0.25D$) and Fig. 13 ($\Delta z = 0.5D$). In Fig. 12, compared to the baseline configuration (isolated rotor), the first three harmonics show reduce levels in both the forward flight and decent cases. There is a clear increase in tonal component levels from the fourth sub-harmonics upward in the forward flight case. Broadband noise is less affected in this case. This suggest that aerodynamic and acoustic interaction effects are central in determining the acoustic radiation above 1 kHz. Results for the decent case show that the shaft angle is also a determinant factor for the acoustic emissions. Here the effect of convection mostly cause an important increase in broadband noise without amplifying the high-frequency tonal components. Above 2.5 kHz an apparent cut-off appears to be reached and the acoustic is dominated by the broadband components.

Doubling the spacing between the rotor to $0.5D$, e.g. Fig. 13, leads to a reduction of the sub-harmonics components in the forward flight case. Although interaction effects are also found to play an important role in determining the acoustic emissions. In the decent case, the effect of convection mostly cause an important increase in broadband noise without having a strong effect on the tonal components.

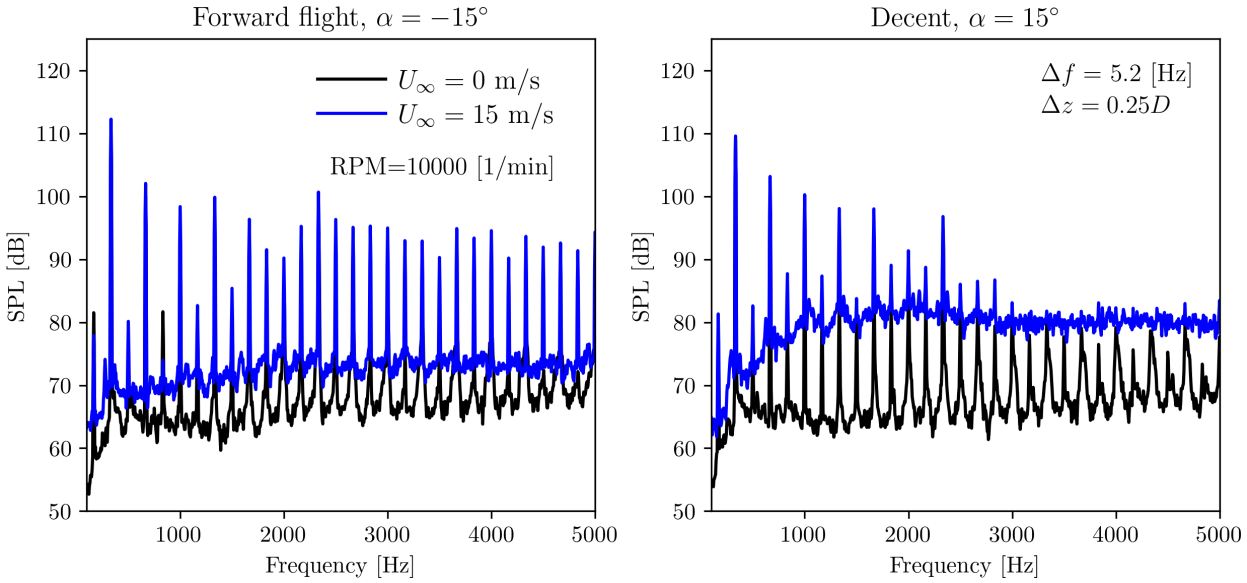


**Fig. 12 Coaxial configuration, $\Delta z = D/4$. Effect of shaft angle and free-stream velocity on the acoustic radiation. Spectral averaging to emphasize the broadband noise component. RPM=10000 1/min, $\theta = -30°$, $R = 0.341$ m.**

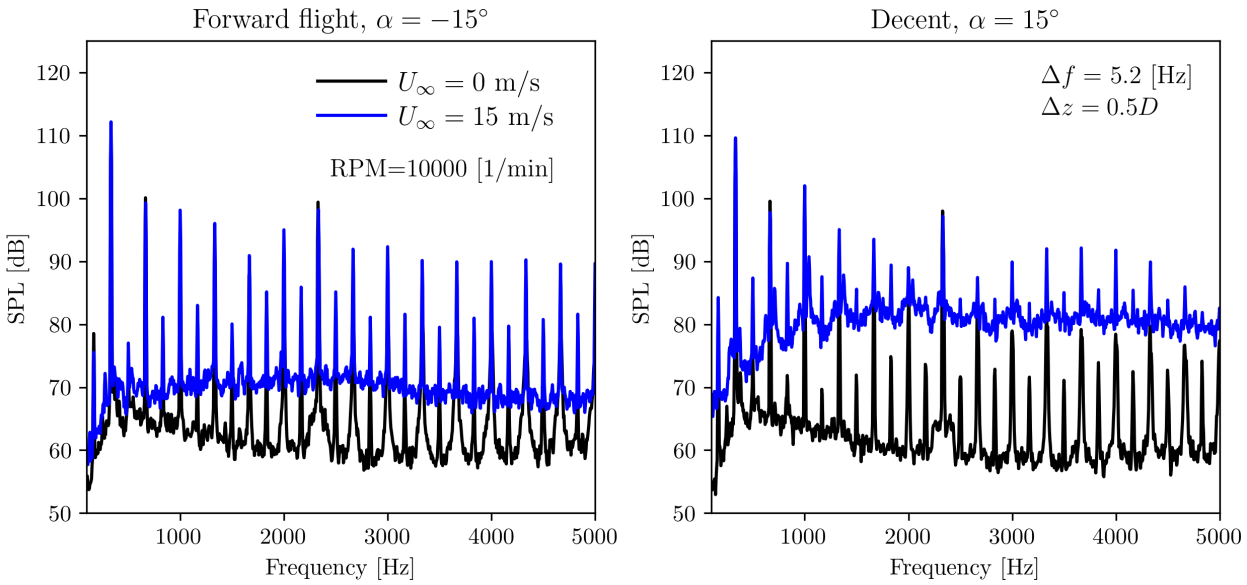


**Fig. 13 Coaxial configuration, $\Delta z = D/2$. Effect of shaft angle and free-stream velocity on the acoustic radiation. Spectral averaging to emphasize the broadband noise component. RPM=10000 1/min, $\theta = -30°$, $R = 0.341$ m.**

### C. Tandem Configuration

Results for the tandem configurations ($\Delta x = 1.18D$, $\Delta y = 0$, $\Delta z = 0$) and ($\Delta x = 1.18D$, $\Delta y = 0.5D$, $\Delta z = 0$) are given in Fig.14 and Fig. 15 respectively. Results for configuration ($\Delta x = 1.18D$, $\Delta y = 0$, $\Delta z = 0.25D$) are provided

in the appendix. For this case, only forward flight data are available. In Fig. 14, both rotors are in the $x-y$ plane aligned with the free-stream direction. Most of the acoustic energy is concentrated in the first few harmonics. Energetic harmonics and sub-harmonics components are still visible up to the 5 kHz limit. A sign that interaction effects are important here a well. Above $\approx$ 2 kHz, motor noise is most probably an important contributor. Increasing the free-stream velocity mostly has an impact on the broadband emissions below 4 kHz, but also on the higher frequency sub-harmonics. In Fig. 15, both rotors are in the $x-y$ plane but separated sideways by $0.5D$ and by $1.18D$ in streamwise direction. In this configuration, an important increase in harmonics and sub-harmonics levels above 1.5 kHz can be observed compared to the data of Fig. 14. At $U_\infty$ = 15 m/s, convection changes the flow dynamics such that most of the high-frequency harmonics are dampened while significantly increasing the low-frequency broadband background noise, e.g. Fig. 7.

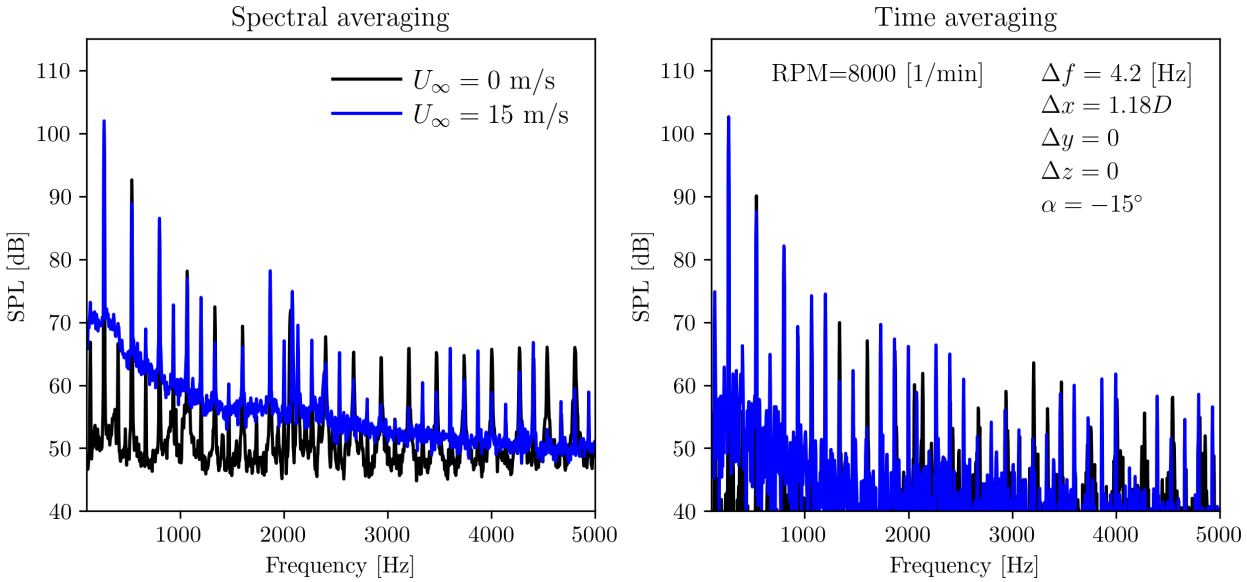


**Fig. 14 Tandem configuration, $\Delta x = 1.18D$, $\Delta y = 0$, $\Delta z = 0$. Effect of free-stream velocity on the acoustic radiation. RPM=8000 1/min, $\theta = -30°$, $R = 0.341$ m.**

## VI. Conclusion

This paper presents a multi-rotor test rig designed for use in the low-speed Acoustic Wind Tunnel Braunschweig of DLR. The test rig is specifically designed to allow the investigation of the aerodynamics and acoustics of small-scale propellers, relevant for urban mobility vehicles applications. The test rig allows testing of isolated rotors, rotors in coaxial configurations and rotors in tandem configurations. The rotors can be freely positioned in all three spatial directions, thus enabling the investigation of aerodynamic and acoustic interaction effects versus lateral, streamwise and vertical separation of the rotors. Through the ability to rotate the rig, the effects of variations in shaft angles can also be investigated.

Details of the rig's instrumentation and electronics are presented to establish the operative range of the setup. Using miniature load cells integrated in the rotor holders, all three force components and moments generated by the rotors can be acquired. The acoustic emission of the rotor configurations, the individual rotor's RPM and the load cells signal acquisition are done synchronously.

Selected results are presented for a single observer position 30° below the rotor plane and for the isolated rotor configuration, the coaxial configuration and the tandem configuration. The results emphasize the impact of aerodynamic and acoustic interaction effects on the characteristics of the acoustics emissions. Multiple rotors in close proximity give rise to the amplification of harmonics and sub-harmonics in the mid- to high-frequency range. Also, in forward decent flight settings, the broadband noise component increase due to the free-stream flow is found to be greater, compared to the isolated rotor configurations.

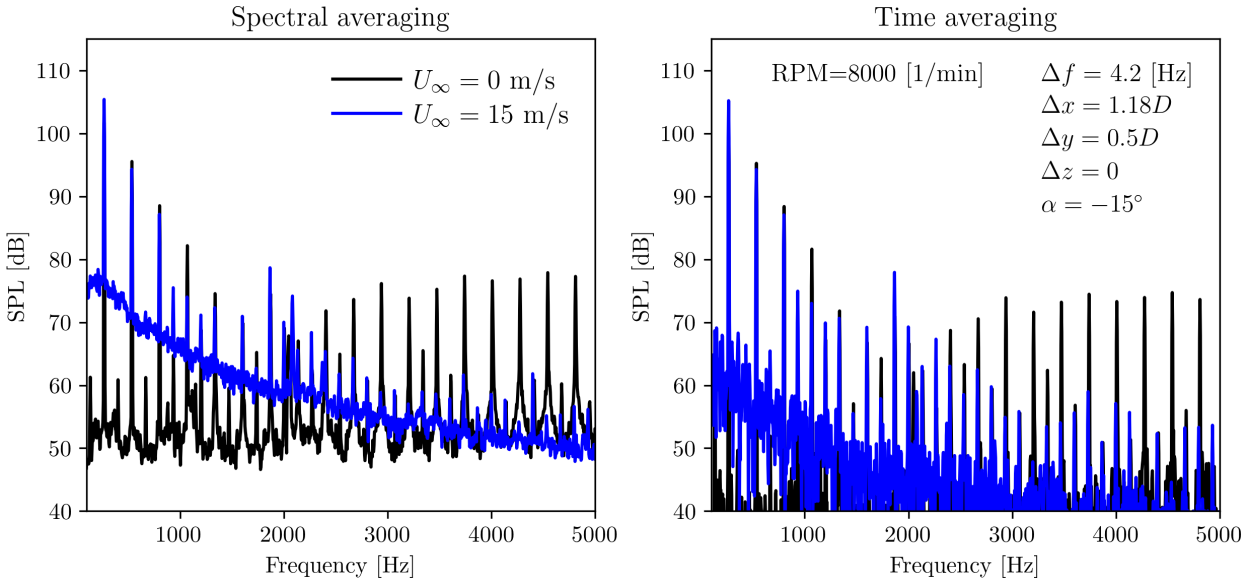


**Fig. 15 Tandem configuration, $\Delta x = 1.18D$, $\Delta y = D/2$, $\Delta z = 0$. Effect of free-stream velocity on the acoustic radiation. RPM=8000 1/min, $\theta = -30°$, $R = 0.341$ m.**

# Appendix

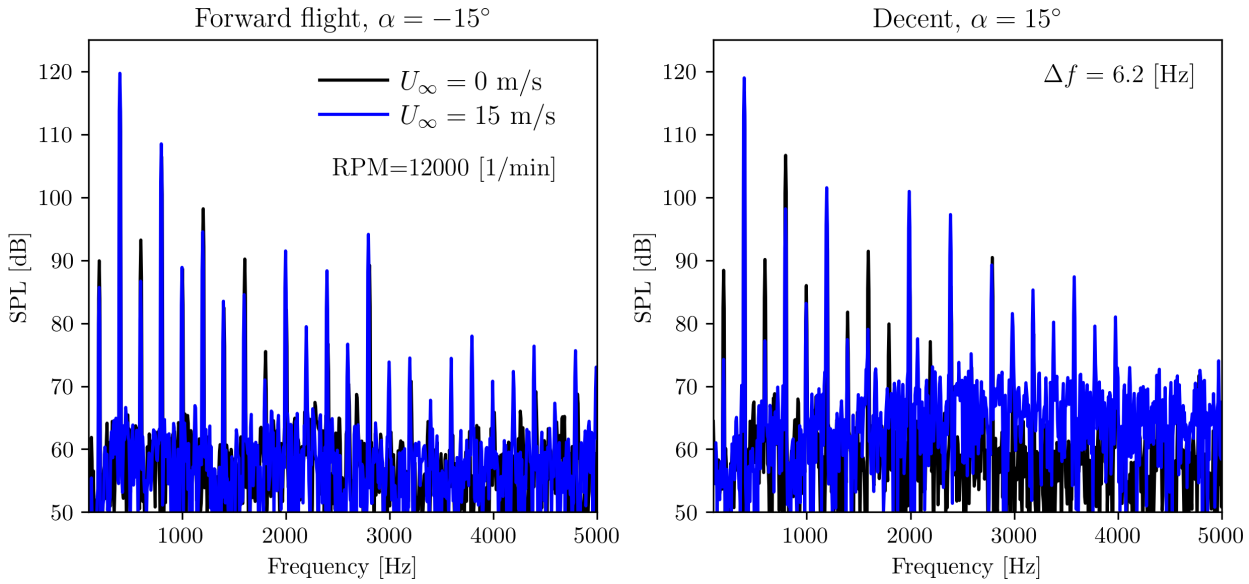


**Fig. 16 Single rotor configuration. Effect of shaft angle and free-stream velocity on the acoustic radiation. Time averaging to emphasize the harmonic components. RPM=12000 1/min, $\theta = -30°$, $R = 0.3$ m.**

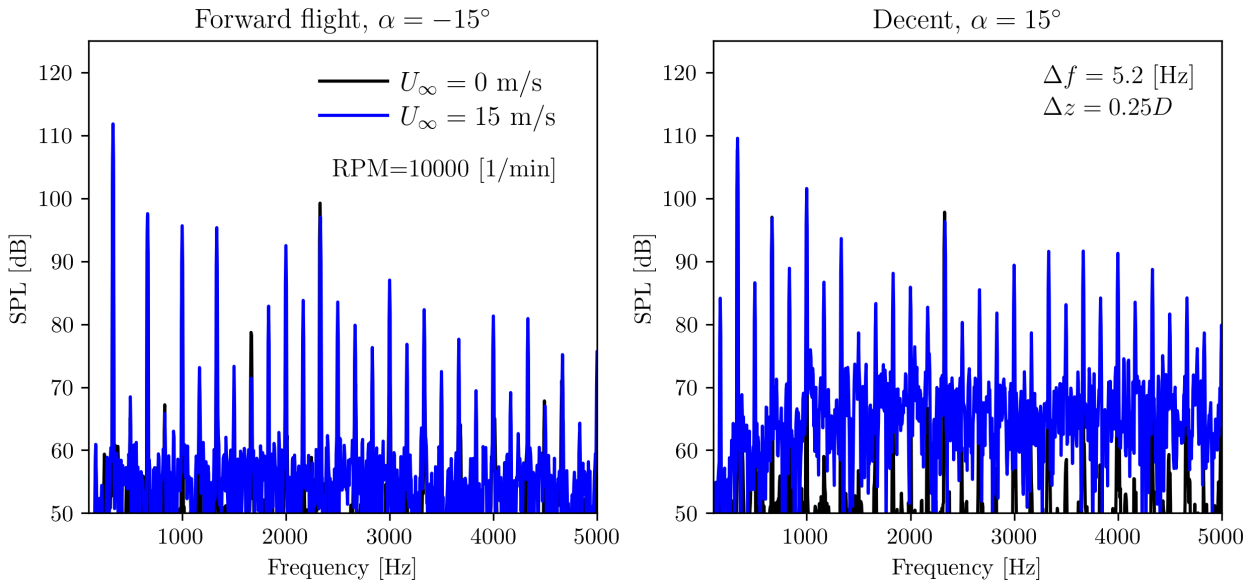


**Fig. 17 Coaxial configuration, $\Delta z = D/4$. Effect of shaft angle and free-stream velocity on the acoustic radiation. Time averaging to emphasize the harmonic components. RPM=10000 1/min, $\theta = -30°$, $R = 0.341$ m.**

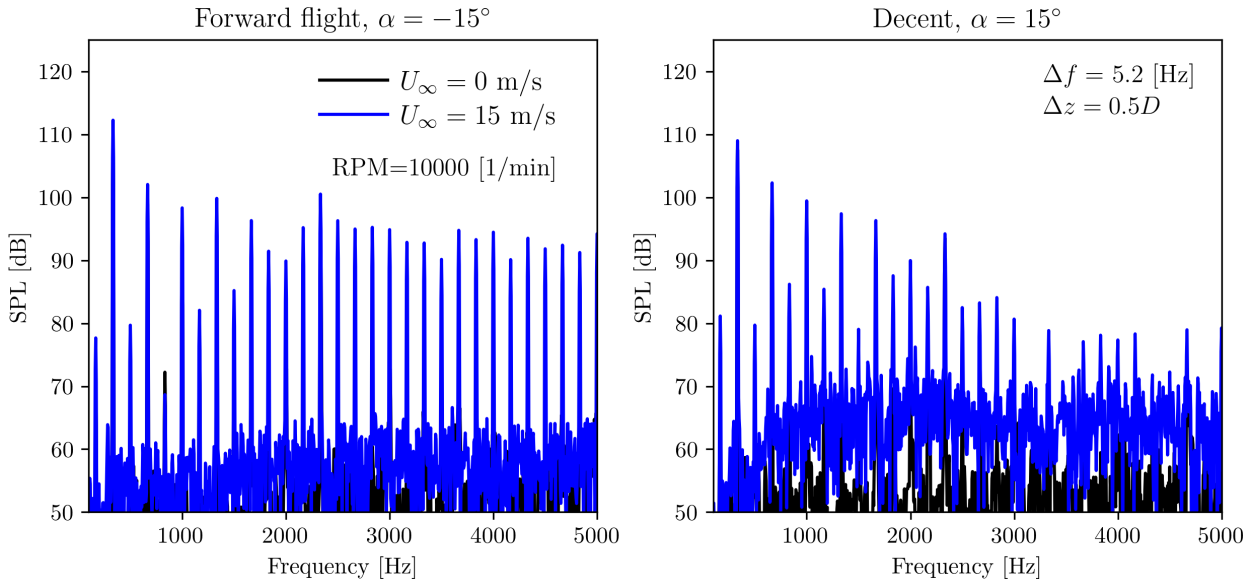


**Fig. 18 Coaxial configuration, $\Delta z = D/2$. Effect of shaft angle and free-stream velocity on the acoustic radiation. Time averaging to emphasize the harmonic components. RPM=10000 1/min, $\theta = -30°$, $R = 0.341$ m.**

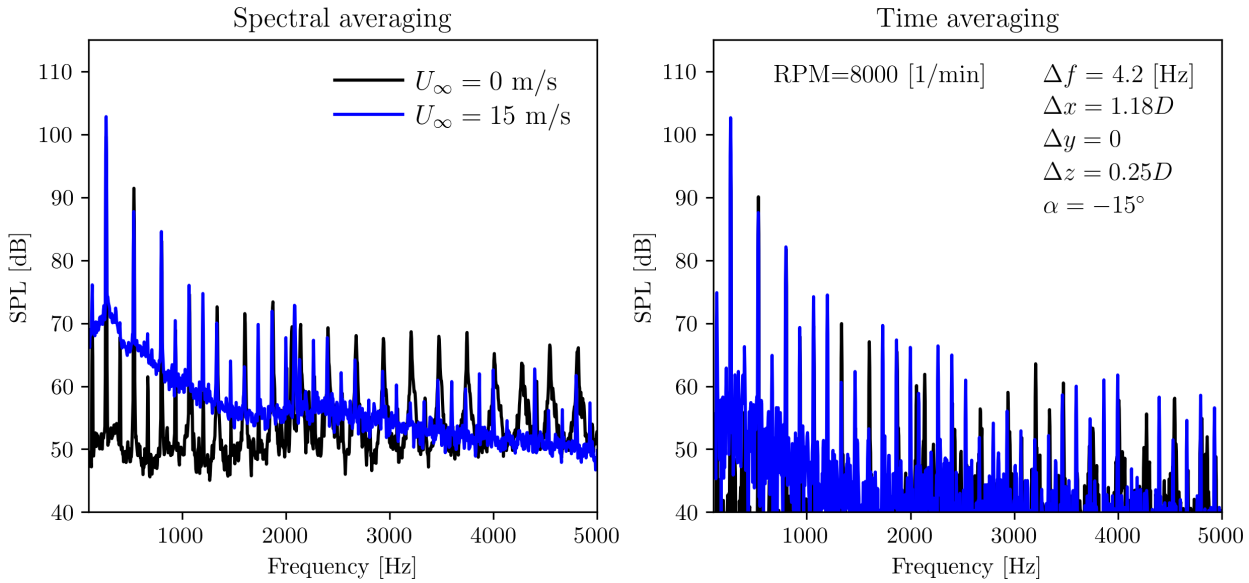


**Fig. 19 Tandem configuration, $\Delta x = 1.18D$, $\Delta y = 0$, $\Delta z = D/4$. Effect of free-stream velocity on the acoustic radiation. Downstream rotor at higher $z$ position as upstream rotor. RPM=8000 1/min, $\theta = -30°$, $R = 0.341$ m.**

## Acknowledgments

The authors would like to acknowledge Bianca Berhorst M. Sc. for conducting the preliminary aerodynamic and acoustic investigations on the test rig.

## References

[1] Straubinger, A., Rothfeld, R., Shamiyeh, M., Büchter, K.-D., Kaiser, J., and Plötner, K. O., "An overview of current research and developments in urban air mobility–Setting the scene for UAM introduction," *Journal of Air Transport Management*, Vol. 87, 2020, p. 101852.

[2] Johnson, W., and Silva, C., "NASA concept vehicles and the engineering of advanced air mobility aircraft," *The Aeronautical Journal*, Vol. 126, No. 1295, 2022, pp. 59–91.

[3] Zawodny, N. S., and Haskin, H., "Small propeller and rotor testing capabilities of the NASA Langley Low Speed Aeroacoustic Wind Tunnel," *23rd AIAA/CEAS Aeroacoustics Conference*, 2017, p. 3709.

[4] Zahirudin, R. A. R., Weitsman, D., Greenwood, E., and Palacios, J., "The Development of a Coaxial Acoustics Test System for Rotor Noise," *77th Annual Vertical Flight Society Forum and Technology Display: The Future of Vertical Flight, FORUM 2021*, Vertical Flight Society, 2021.

[5] Pott-Pollenske, M., and Delfs, J., "Enhanced capabilities of the aeroacoustic wind tunnel Braunschweig," *14th AIAA/CEAS Aeroacoustics Conference (29th AIAA Aeroacoustics Conference)*, 2008, p. 2910.